Inorganic Materials, Vol. 41, No. 6, 2005, pp. 627–638. Translated from Neorganicheskie Materialy, Vol. 41, No. 6, 2005, pp. 720–732.

Crystal–Melt Partition Coefficients of Impurities in Forsterite, Mg_2SiO_4: Experimental Determination, Crystal-Chemical Analysis, and Thermodynamic Evaluation

V. B. Dudnikova[1], V. S. Urusov[1,2], and E. V. Zharikov[3,4]

[1] *Vernadsky Institute of Geochemistry and Analytical Chemistry, Russian Academy of Sciences, ul. Kosygina 19, Moscow, 119991 Russia*

[2] *Moscow State University, Vorob'evy gory 1, Moscow, 119899 Russia*

[3] *Laser Materials and Technologies Research Center, Prokhorov General Physics Institute, Russian Academy of Sciences, ul. Vavilova 38D, Moscow, 119991 Russia*

[4] *Mendeleev University of Chemical Technology, Miusskaya pl. 9, Moscow, 125047 Russia*

e-mail: vdudnikova@mtu-net.ru

Received July 7, 2004

Abstract—The forsterite–melt partition coefficients K are determined experimentally for a large number of mono-, di-, tri-, and tetravalent impurities. The energies of native defects and impurities (E_d) and the solution energies (E_s) of impurities in forsterite are evaluated using computer simulation. The defect energy is shown to vary linearly with the difference in ionic radius between the host and substituent atoms (Δr) and with the impurity cation charge, while the partition coefficient and solution energy of impurities are quadratic functions of these parameters. The plots of $\ln K$ versus $(\Delta r)^2$ and E_s versus $(\Delta r)^2$ for isovalent substitutions ($Me^{\times}_{Mg}$ and $Me^{\times}_{Si}$) pass close to the origin, in contrast to the plots for heterovalent substitutions ($Me^{'}_{Mg}$ and $Me^{\cdot}_{Si}$). The significant y intercept of the latter plots is interpreted as evidence for the formation of extra defects maintaining electroneutrality. The y intercept of the plot of E_s versus $(\Delta r)^2$ is 2 eV, which is about half the formation energy of Frenkel defects in forsterite. The best fit equations representing the correlation between the partition coefficients and solution energies of impurities demonstrate that heterovalent substitutions increase the entropy contribution to the free energy of solution of impurities.

INTRODUCTION

Data on crystal–melt partitioning of elements are crucial for understanding the nature of chemical differentiation in crystallization processes and enable controlled doping of synthetic crystals and the preparation of materials with tailored properties. Experimental studies demonstrate that the partition coefficient of impurities depends on their atomic radius and charge, temperature, pressure, crystal composition, and, in the case of elements of variable valence, on the oxygen fugacity at which crystallization occurs.

Experimental determination of the partition coefficient K requires, in some cases, considerable effort and time. Thermodynamic evaluation of K was successfully used in many studies dealing with crystallization of alkali halides (see, e.g., [1, 2]) and oxide and silicate systems [2]. Significant advances have been made to date in computer simulation of structures, which allows the solution energies E_s of impurities to be estimated [3]. In the case of forsterite, however, the solution energies of tetravalent impurities and those of mono- and trivalent impurities self-compensated by native defects have not yet been reported. Calculated E_s values are difficult to convert to K because it is necessary to take into account the effects of temperature, defect density, the entropy contribution to the solution energy, and the properties of the melt. The most accurate evaluation of K is ensured by molecular dynamics simulation (Monte Carlo method) [4]. This approach is, however, also confronted with a number of limitations and unresolved problems.

Correlation approaches allow one to systematize available information, predict unknown K, and correct data that are inconsistent with the general trend. In a number of systems, K was found to correlate with the impurity solubility in the crystalline phase, standard electrode potential of the impurity, its melting point, lattice energy, and diffusion coefficient in the host crystal [1, 5]. A strong correlation was also found between K and the difference in ionic radius (Δr) between the host atoms and the substituent. Onuma *et al.* [6] fitted experimental data to a parabolic relation between $\ln K$ and the ionic radius of the impurity. The parabolic relation between $\ln K$ and Δr was confirmed in many studies by analyzing impurity partitioning for a wide variety of inorganic substances and minerals [2, 3, 7–17].

0020-1685/05/4106-0627

Table 1. Forsterite–melt partition coefficients of impurities

Impurity	r, Å	C_{L_0}, wt %	K	ΔK	Analytical technique
Monovalent impurities					
Li	0.76	0.2	0.007	0.001	ICP OES, FOES
Divalent impurities					
Ni	0.69	0.8–3.3	0.75	0.04	EPXMA
Co	0.745	0.18–0.2	0.53	0.04	EPXMA
Mn	0.83	1.0	0.39	0.02	EPXMA
Ca	1.0	1.12	0.073	0.005	EPXMA
Sr	1.18	1.22	0.0007	0.0002	AA
Ba	1.35	1.44–1.91	0.0004	0.0002	ICP OES
Trivalent impurities					
Cr	0.615	0.14	0.18	0.018	EPXMA
Ga	0.62	4.4×10^{-4}	0.055	0.009	NAA
Sc	0.745	2.8×10^{-4}	0.19	0.02	NAA
Lu	0.861	1×10^{-3}	0.1	0.01	NAA
Er	0.89	0.4–0.6	0.02	0.002	EPXMA
Gd	0.938	4.9×10^{-3}	0.022	0.003	NAA
Eu	0.947	9.4×10^{-4}	0.0054	0.0009	NAA
Sm	0.958	1×10^{-3}	0.007	0.001	NAA
Nd	0.983	0.17–0.19	0.002	0.0005	NAA
La	1.032	8×10^{-4}	0.002	0.0007	NAA
Tetravalent impurities					
Ti	0.42	0.34–0.67	0.06	0.003	ICP OES, EPXMA
V	0.46	0.35–2	0.07	0.005	EPXMA
Hf	0.58	1.25	0.0017	0.0008	NAA
Zr	0.59	0.65–1.26	0.002	0.0008	ICP OES, NAA

Experimentally determined partition coefficients can also be fitted to a cubic relation between K and the ionic radius of the impurity (difference in atomic volume between the host atoms and the substituent) [18].

In this paper, we report experimental data on forsterite–melt partition coefficients of impurities and analyze in detail the effects of the ionic radius and charge state of impurities on K. The experimental data are compared with computer simulation results on native and impurity defects in forsterite in order to correlate the experimentally determined macroscopic properties of impurities with their calculated solution energy.

EXPERIMENTAL DETERMINATION OF THE FORSTERITE–MELT PARTITION COEFFICIENTS OF IMPURITIES

Forsterite single crystals (melting point, 1890°C) were grown by the Czochralski technique. The growth charge was prepared by reacting stoichiometric mixtures of extrapure-grade SiO_2 and MgO at 1200°C for 24 h and was then pressed into pellets. Impurities were introduced into the growth charge in the form of oxides or carbonates. The crystals were pulled from Ir crucibles in an inert atmosphere, using single-crystal forsterite seeds oriented in the [010] direction (*Pnma* setting). For some elements of variable valence, growth runs were carried out under different redox conditions. Oxygen fugacity was varied in the range $-4 \le \log f_{O_2} \le -0.9$. The rotation rate was 12–20 rpm. In most growth runs, the pulling rate was 2 mm/h. In a number of experiments, the pulling rate was increased to 7 mm/h in order to assess its effect on K. The grown crystals were cooled at a rate of about 100°C/h. The fraction of the solidified melt was typically within 5–10%.

The impurity concentration in the crystals was determined by electron probe x-ray microanalysis (EPXMA) on a CAMEBAX x-ray microanalyzer, neutron activation analysis (NAA), ICP optical emission spectroscopy (ICP OES), atomic absorption (AA), and flame OES (FOES).

According to EPXMA and chemical analysis data, the pure forsterite crystals had the stoichiometric cation composition. The crystals contained iridium impurity (2–10 ppm as determined by NAA), which originated from the crucible material. The impurities were typically uniformly distributed over the length of the crystal because the fraction of the solidified melt was rather small. We also determined the impurity concentration in the residual melt after crystal growth in order to assess impurity losses through vaporization. In addition, we compared the impurity concentrations in crystals prepared in several consecutive growth runs. In most growth runs, impurity losses from the melt were insignificant, except for nickel: according to EPXMA and NAA data for the residual melt, about 20% of the Ni was lost through vaporization in each growth run.

The partition coefficient K was evaluated by extrapolating C_S/C_{L_0} to $g = 0$, where C_S is the impurity concentration in the crystal, C_{L_0} is the initial impurity concentration in the melt, and g is the fraction of the solidified melt. Note that the growth rate had little effect on the partition coefficient.

The experimental results are presented in Table 1 together with earlier reported data [10, 19]. The partition coefficients of Sr, Ba, and tetravalent impurities are reported for the first time. Table 1 lists Shannon's ionic radii r of impurities [20], initial impurity concentrations in the melt C_{L_0}, partition coefficients K, confidence intervals ΔK, and analytical techniques used.

For ions of variable valence, K may depend on oxygen fugacity because of changes in the relative amounts of different valence states. In studies of the vanadium and chromium solubilities in forsterite, oxygen fugacity during crystal growth was varied in the range $-4 \le$

$\log f_{O_2} \le -0.92$. The forsterite–melt partition coefficient of vanadium was determined to be 0.07. K_V was independent of oxygen fugacity because most of the vanadium in the range of oxygen fugacities studied was in the oxidation state 4+ [21]. At the same time, the partition coefficient of chromium, present mainly as Cr^{3+} and Cr^{4+}, varied from 0.18 to 0.09. According to earlier experimental studies [22], $K_{Cr} = 0.18$ for crystals containing chromium mainly in the form of Cr^{3+} ions (at $f_{O_2} = 10^{-4}$). Note that, according to Shenjun *et al.* [23], forsterite crystals grown in an inert atmosphere contain titanium mainly in the form of Ti^{4+} ions.

Comparison of our results with the data reported by Kobayashi and Takei [24], who determined the partition coefficients of several trivalent impurities in forsterite, indicates that, in most cases, their values of K are slightly higher (Fig. 1), presumably because Kobayashi and Takei [24] added Na^+ ions, which may act as charge compensators.

CRYSTAL-CHEMICAL ANALYSIS OF IMPURITY PARTITION COEFFICIENTS

The experimentally determined values of K are presented in Fig. 1 as a function of the difference in ionic radius between the host cations and the substituent. Δr was determined under the assumption that di- and trivalent ions in forsterite substitute on the magnesium (octahedral) site, while tetravalent impurities substitute on the silicon (tetrahedral) site.

For a given valence, $\ln K$ is a linear function of $(\Delta r)^2$ (Fig. 2), with the best fit equations

$$\ln K = -31.91(\Delta r)^2 - 0.41 \text{ for } Me^{2+},$$

$$\ln K = -47.44(\Delta r)^2 - 1.23 \text{ for } Me^{4+},$$

$$\ln K = -50.68(\Delta r)^2 - 1.96 \text{ for } Me^{3+}.$$

The only exception is the forsterite–melt partition coefficient of barium, which is larger than would be expected from the general trend for divalent ions. The increased value of K_{Ba} may be due to difficulties in detecting low-solubility impurities and also to microimpurity trapping [2], which is very likely for impurities differing markedly in properties from the host.

At a given ionic radius, the forsterite–melt partition coefficient decreases in the order $Me^{2+} > Me^{4+} > Me^{3+} > Me^+$, which provides further evidence that isovalent substitutions are energetically more favorable than heterovalent substitutions. The Li^+ ion, which is close in size to Mg^{2+} (0.76 and 0.72 Å, respectively) but has a lower valence, has the lowest K among the heterovalent substitutions considered. This is in line with Goldschmidt's isomorphism polarity rule [11], which states

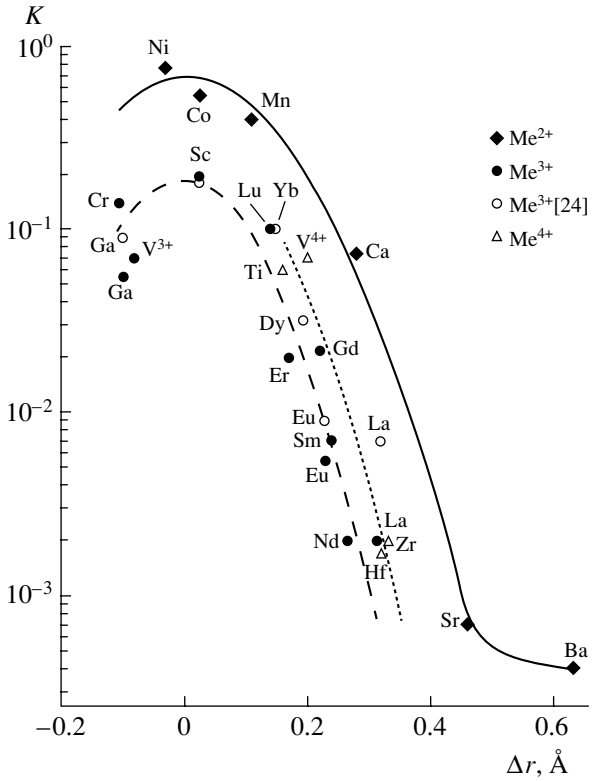

Fig. 1. Forsterite–melt partition coefficients of impurities vs. difference in ionic radius between the host cations and the substituent (Onum curves).

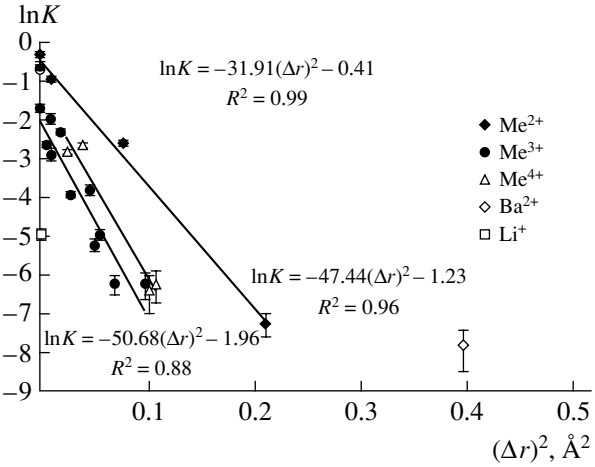

Fig. 2. Plots of $\ln K$ vs. $(\Delta r)^2$ for different valence states of impurities; R^2 is the goodness-of-fit index.

that ions in higher charge states are incorporated into crystals more readily.

Figure 3 shows the variation of K with the charge of cations substituting for Mg. The solid line represents data for $\Delta r = 0.04$ Å, where we use the experimentally determined K_{Li} and the values of K for di- and trivalent impurities estimated using correlation equa-

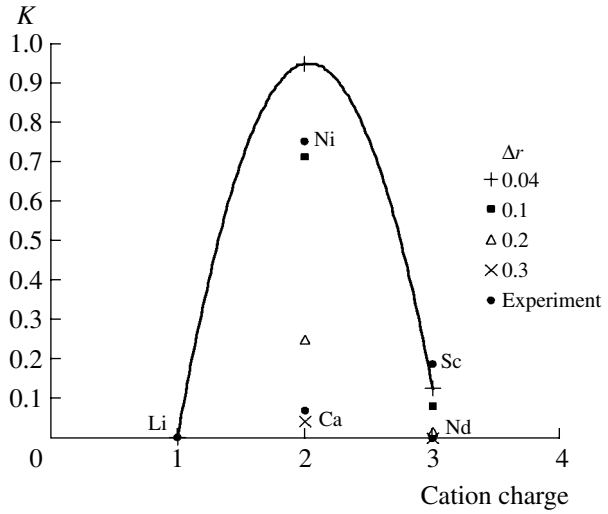

Fig. 3. Variation of K with the charge of cations substituting for Mg^{2+} in forsterite crystals at different values of Δr.

tions. The same equations were used to calculate K for di- and trivalent impurities with Δr from 0.1 to 0.3. In addition, Fig. 3 presents the experimental data for impurities close in size to the Mg^{2+} ion (Li, Ni, and Sc; $\Delta r \le 0.04$ Å) and for impurities differing substantially in size from Mg^{2+} (Ca and Nd, $\Delta r = 0.28$ and 0.26 Å, respectively). As seen, K varies parabolically with cation charge. With increasing Δr, the parabola becomes flatter. The parabolic variation of the partition coefficient with the charge of cations substituting on the M2 site of clinopyroxene was reported by Wood and Blundy [25].

DEFECT FORMATION AND INTERACTION IN THE FORSTERITE–MELT SYSTEM

The forsterite structure is made up of isolated zigzag chains formed by Mg octahedra and running along the b axis (Fig. 4). Each M1 octahedron share edges with two M1 and two M2 octahedra. Each M2 octahedron share edges with two M1 octahedra. Within each layer, the chains of Mg octahedra are separated by similar chains of octahedral interstices, M3 and M4. Adjacent layers are displaced relative to one another so that the occupied Mg chains of the upper layer reside over the chains of interstices of the lower layer, and vice versa [26]. The chains of occupied octahedra in the first and third layers are linked by S1 silicon tetrahedra and separated by S2 and S3 tetrahedral interstices.

Impurity dissolution in forsterite can be considered in terms of exchange reactions between the crystalline phase and the melt containing the host and guest cations in the form of ionic oxides. Isovalent substitutions of Me^{2+} for Mg^{2+} can be represented by the quasi-chemical reaction[1]

$$Mg_{Mg}^{\times} + MeO \rightleftharpoons Me_{Mg}^{\times} + MgO. \quad (1)$$

For Me^{4+} ions on the Si site, we have

$$Si_{Si}^{\times} + MeO_2 \rightleftharpoons Me_{Si}^{\times} + SiO_2. \quad (2)$$

The solution energies E_s of impurities in reactions (1) and (2) can be found as

$$E_s(Me^{2+}) = E_d(Me_{Mg}^{\times}) + E_l(MgO) - E_l(MeO), \quad (3)$$

$$E_s(Me^{4+}) = E_d(Me_{Si}^{\times}) + E_l(SiO_2) - E_l(MeO_2), \quad (4)$$

where E_d is the energy of impurity defects ($Me_{Mg}^{\times}$ or $Me_{Si}^{\times}$) in forsterite and E_l is the lattice energy of pure oxides.

Heterovalent substitution of Me^{+} or Me^{3+} for Mg^{2+} leads to the formation of an impurity defect carrying an excess positive or negative charge, which must be compensated. Charge compensation may occur by different mechanisms. The excess negative charge of a monovalent impurity in forsterite can be compensated by native defects (oxygen vacancies $V_O^{\bullet\bullet}$ and magnesium interstitials $Mg_i^{\bullet\bullet}$):

$$\frac{1}{2}Me_2O + Mg_{Mg}^{\times} + \frac{1}{2}O_O^{\times} \rightleftharpoons Me'_{Mg} + \frac{1}{2}V_O^{\bullet\bullet} + MgO, \quad (5)$$

$$\frac{1}{2}Me_2O + Mg_{Mg}^{\times} \rightleftharpoons Mg'_{Mg} + \frac{1}{2}Mg_i^{\bullet\bullet} + \frac{1}{2}MgO. \quad (6)$$

The excess positive charge of trivalent impurities may be compensated through the process

$$\frac{1}{2}Me_2O_3 + \frac{3}{2}Mg_{Mg}^{\times} \rightleftharpoons Me_{Mg}^{\bullet} + \frac{1}{2}V''_{Mg} + \frac{3}{2}MgO, \quad (7)$$

where V''_{Mg} is a magnesium vacancy. Also possible is charge compensation via combined substitution of mono- and trivalent ions on the Mg site,[2]

$$\frac{1}{2}Me_2O_3 + \frac{1}{2}\mathbf{Me}_2O + 2Mg_{Mg}^{\times} \rightleftharpoons \mathbf{Me}'_{Mg} + Me_{Mg}^{\bullet} + 2MgO, \quad (8)$$

[1] Hereafter, we use standard Kröger notation: subscripts specify lattice sites, and superscripts indicate an excess positive (●) or negative (') charge relative to the charge of the ion on its own site (×); V is a vacancy.

[2] To differentiate impurity ions in Eqs. (8), (9), (13), (14), and (16), one of them is designated **Me**.

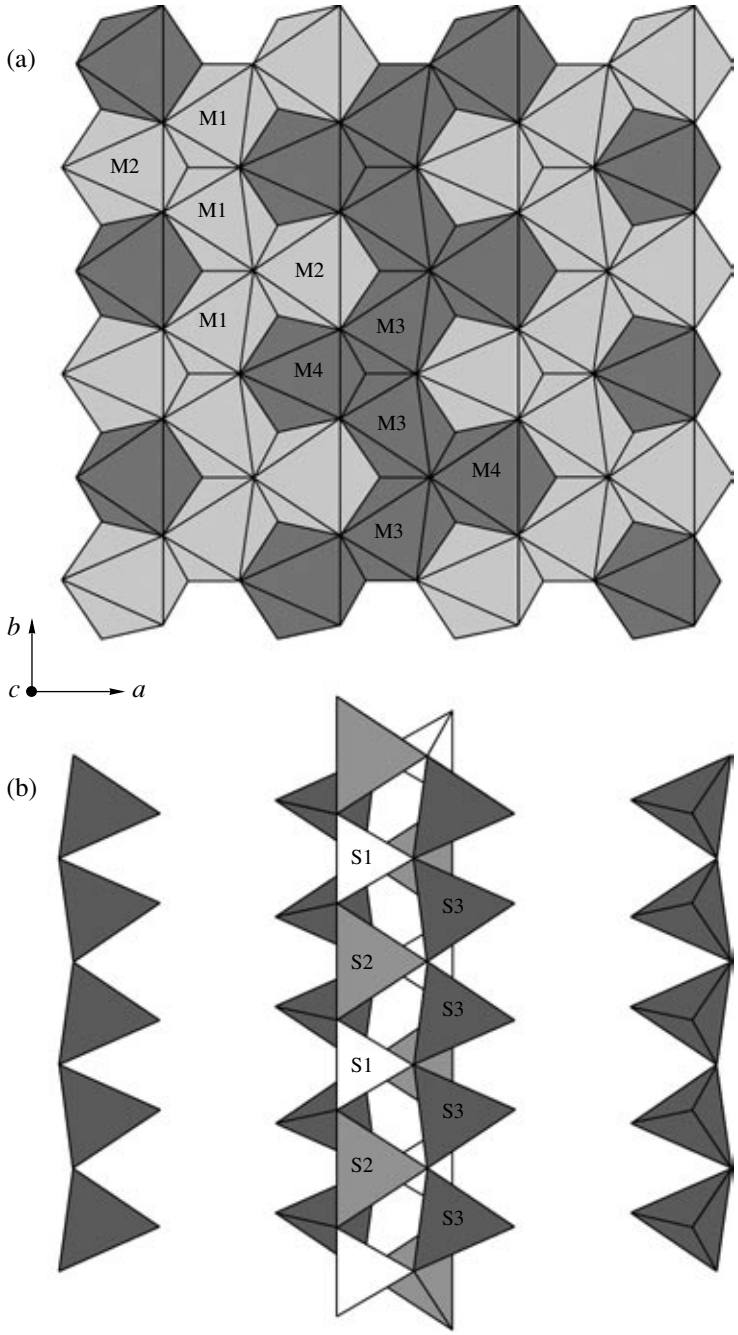

Fig. 4. Forsterite structure: (a) occupied (M1, M2) and vacant (M3, M4) octahedral sites, (b) occupied (S1) and vacant (S2, S3) tetrahedral sites.

or two trivalent ions on the Mg and Si sites,

$$\frac{1}{2}Me_2O_3 + \frac{1}{2}\mathbf{Me}_2O_3 + 2Mg_{Mg}^{\times} + Si_{Si}^{\times} \rightleftharpoons \mathbf{Me}'_{Si} + Me^{\bullet}_{Mg} + 2MgO + SiO_2. \quad (9)$$

The solution energies for reactions (5)–(9) can be evaluated by the equations

$$E_s(Me^+) = E_d(Me'_{Mg}) + \frac{1}{2}E_d(V_O^{\bullet\bullet}) + E_l(MgO) - \frac{1}{2}E_l(Me_2O), \quad (10)$$

$$E_s(Me^+) = E_d(Me'_{Mg}) + \frac{1}{2}E_d(Mg_i^{\bullet\bullet}) + E_l(MgO) - \frac{1}{2}E_l(Me_2O), \quad (11)$$

$$E_s(Me^{3+}) = E_d(Me^{\cdot}_{Mg}) + \frac{1}{2}E_d(V''_{Mg}) + \frac{3}{2}E_l(MgO) - \frac{1}{2}E_l(Me_2O_3), \quad (12)$$

$$E_s(Me^{3+}, \mathbf{Me}^{+}) = E_d(Me^{\cdot}_{Mg}) + E_d(\mathbf{Me}'_{Mg}) + 2E_l(MgO) - \frac{1}{2}E_l(Me_2O_3) - \frac{1}{2}E_l(\mathbf{Me}_2O), \quad (13)$$

$$E_s(Me^{3+}, \mathbf{Me}^{3+}) = E_d(Me^{\cdot}_{Mg}) + E_d(\mathbf{Me}'_{Si}) + 2E_l(MgO) + 2E_l(SiO_2) - \frac{1}{2}E_l(Me_2O_3) - \frac{1}{2}E_l(\mathbf{Me}_2O_3). \quad (14)$$

As is well known, charged defects may form defect complexes, e.g.,

$$2Me^{\cdot}_{Mg} + V''_{Mg} \rightleftharpoons (Me_{Mg}V_{Mg}Me_{Mg})^{\times}, \quad (15)$$

$$Me^{\cdot}_{Mg} + \mathbf{Me}'_{Mg} \rightleftharpoons (Me_{Mg}\mathbf{Me}_{Mg})^{\times}. \quad (16)$$

In calculating the solution energy of impurities, one must then use the energies of defect complexes instead of the energies of noninteracting defects.

COMPUTER SIMULATION OF DEFECTS IN FORSTERITE CRYSTALS

The energies of defects in forsterite can be assessed using computer simulation, which allows one to calculate the energy of an optimized structural model. The energy of a point defect depends on its interaction with the surrounding host material and can be found by minimizing the static energy of the crystal while varying the positions of the atoms and dipole moments around the defect. It is equal to the difference between the energy of the crystal distorted by the defect and the energy of a defect-free crystal.

In the Mott–Littleton model, the crystal is divided into two regions: region I comprises the defect and its immediate neighborhood, and region II is the rest of the crystal. The displacements and dipole moments in the inner region are evaluated by considering interionic interactions, while the outer region is treated as a continuous dielectric medium. Calculations are performed in a static approximation for infinite dilution. Region I in our simulations was 10 Å in size (638 ions).

Table 2. Parameters of interatomic potentials for forsterite

Interaction	B, eV	λ, Å	c, eV Å^6
Si–O	1283.9073	0.3205	10.6616
Mg–O	1428.5	0.2945	0
O–O	22764.3	0.149	27.88
O–Si–O	α = 2.097 eV/rad^2		
O_c–O_s	χ = 74.9204 eV/Å^2		

Note: O_c is the core of an oxygen ion, and O_s is its valence shell.

The simulations were carried out in an ionic approximation, using the General Utility Lattice Program (GULP) [27]. The pair potential for ions i and j with charges q_i and q_j had the form

$$U_{ij}(R_{ij}) = q_iq_je^2/R_{ij} + B_{ij}\exp(-R_{ij}/\lambda_{ij}) - c_{ij}/R_{ij}^6. \quad (17)$$

The first term in (17) represents the energy of Coulombic interaction, the second term represents repulsion due to the overlap of the electron shells of neighboring atoms, and the third term takes into account van der Waals interaction. R_{ij} is the interatomic distance, and B_{ij}, λ_{ij}, and c_{ij} are the parameters of the short-range potentials. The parameters of the potentials for Me–O interactions were taken from [28–30]. The parameters for pure forsterite are listed in Table 2.

It is well known that the chemical bonding in Mg_2SiO_4 cannot be adequately described in a purely ionic approximation. One effective way to take into account covalent bonding is to allow for the polarizability of individual atoms, most frequently anions.

The polarizability of the oxygen ion is usually described in the so-called "shell model." In this approach, the ion is thought of as a core in which the entire mass is concentrated. The core is surrounded by a charged shell which represents valence electrons. The core and shell are linked by a harmonic elastic constant χ_i,

$$U_i^s = \frac{1}{2}\chi_i l_i^2, \quad (18)$$

where l_i is the distance between the core and the center of the displaced shell.

Three-particle interaction was taken into account by introducing the bond angle potential of the directional, partially covalent bond O–Si–O (ions i, j, and k),

$$U_{ijk} = \frac{1}{2}\alpha_{ijk}(\theta_{ijk} - \theta_0)^2, \quad (19)$$

where α_{ijk} is a constant, θ_{ijk} is the equilibrium bond angle, and θ_0 = 109.47° is the ideal tetrahedral bond angle. The values of χ and α were taken from Sanders *et al.* [30] (Table 2).

The simulation results for the forsterite structure are summarized in Tables 3 and 4. The computed atomic positional parameters, lattice parameters, and unit-cell volume were compared with experimental data [31]. The discrepancy between the computed and measured lattice parameters was less than 1%, and that between the computed and measured unit-cell volumes was 1.5%. The largest difference in positional parameters was 5%.

The computed energies of native defects in forsterite are listed in Table 5. The lowest defect energies are indicated in bold type. Clearly, the corresponding defect species are the most energetically favorable and must be present in the highest concentrations.

The M1 site is more favorable for Mg vacancies than is M2. Oxygen vacancies are formed more readily in the O3 site. The O1 site is the least favorable because of the short Si–O1 bond. The energies of magnesium and oxygen vacancies (V''_{Mg} and $V_O^{\bullet\bullet}$) differ little, while that of Si vacancies ($V_{Si}^{\bullet\bullet\bullet\bullet}$) is higher by a factor of 4. Oxygen interstitials and Si vacancies are unlikely in forsterite [32].

In the case of Mg ions, the formation energy of Frenkel defects, $0 \rightleftharpoons V''_{Mg} + Mg_i^{\bullet\bullet}$, per particle can be estimated using the relation

$$E_F = \frac{1}{2}[E_d(V''_{Mg}) + E_d(Mg_i^{\bullet\bullet})]. \quad (20)$$

In this way, we obtain $E_F = 3.7$ eV (Table 5).

The formation energy of Schottky defects per Mg_2SiO_4 formula unit can be found as

$$E_{Sch} = \frac{1}{7}[(2E_d(V''_{Mg}) + E_d(V_{Si}^{\bullet\bullet\bullet\bullet}) + 4E_d(V_O^{\bullet\bullet}) - E_l(Mg_2SiO_4)]. \quad (21)$$

We obtain $E_{Sch} = 5.9$ eV. Comparison with E_F indicates that the formation of Frenkel defects is energetically far more favorable in comparison with Schottky defects.

The energies of native defects listed in Table 5 agree well with experimental data and other calculations [33, 34]. The formation energy of Mg interstitials $Mg_i^{\bullet\bullet}$ in the M3 site is calculated in this work for the first time.

Table 6 lists the parameters of Me–O interatomic potentials used for impurity centers and the calculated defect energies E_d and solution energies E_s of impurities in forsterite. Also given in Table 6 are the lattice energies E_l of Me_tO_y oxides. The E_l of MgO is –41.3 eV, and that of SiO_2 is –128.7 eV. The lattice energies of pure oxides were calculated using the same repulsion parameters as in the case of the energies of the corresponding defects in forsterite, which was expected to cancel the errors due to the ionic approximation.

The data in Table 6 agree with the simulation results reported by Purton *et al.* [35, 36] to within tenths of an electronvolt except for Ca, Sr, and Ba impurities, for which the difference in E_d is 1.0, 2.8, and 5.8 eV, respectively. The likely reason for these discrepancies is that different parameters of the repulsion potential were used. Therefore, the choice of these parameters is still open to question. At the same time, owing to the above-mentioned compensation of errors, the differences in E_s are as small as a fraction of an electronvolt, which indicates that matched repulsion parameters must be used in simulation.

It follows from the simulation results that the M1 site is energetically more favorable for monovalent

Table 3. Calculated and measured lattice parameters of forsterite (sp. gr. *Pnma*, $Z = 4$)

Parameter	Calculation	Experiment [31]
a, Å	10.24	10.18
b, Å	5.985	5.976
c, Å	4.781	4.746
V, Å^3	293.11	288.60

Table 4. Calculated and measured atomic positional parameters in the structure of forsterite

Atom	x	y	z	x	y	z
	calculation			experiment [31]		
Mg(M1)	0.0000	0.0000	0.0000	0.0000	0.0000	0.0000
Mg(M2)	0.2830	0.2500	0.9978	0.2772	0.2500	0.9914
Si	0.0979	0.2500	0.4452	0.0939	0.2500	0.4261
O(1)	0.0924	0.2500	0.7841	0.0919	0.2500	0.7661
O(2)	0.4529	0.2500	0.2100	0.4469	0.2500	0.2202
O(3)	0.1646	0.0344	0.2934	0.1628	0.0333	0.2777

Table 5. Native defects in forsterite crystals

Defect	Position	E_d, eV
V''_{Mg}	M1	**24.5**
	M2	26.4
$Mg_i^{\bullet\bullet}$	M3	–11.5
	M4	**–17.1**
V_{Si}''''	S1	103.2
$Si_i^{\bullet\bullet\bullet\bullet}$	S2	–77.6
	S3	**–79.0**
$V_O^{\bullet\bullet}$	O1	28.0
	O2	25.2
	O3	**24.4**
Mg-related Frenkel defect		$E_F = 3.7$ eV
Schottky defect		$E_{Sch} = 5.9$ eV

Table 6. Parameters of interatomic potentials and calculated defect energies E_d and solution energies E_s of impurities in forsterite

Me	Δr, Å	B, eV	λ, Å	E_d, eV		E_l, eV	E_s, eV	
				M1	M2	Me_iO_y	M1	M2
Monovalent impurities								
Li	0.04	292.3	0.3472	**16.80**	17.40	–29.10	**2.16**	2.76
Na	0.3	611.1	0.3535	**19.70**	20.00	–24.90	**2.96**	3.26
K	0.66	902.8	0.3698	**23.30**	23.40	–22.20	**5.21**	5.31
Rb	0.8	1010.8	0.3793	25.20	**25.19**	–21.20	6.61	**6.60**
Divalent impurities								
Ni	–0.03	1582.5	0.2882	**–0.34**	–0.31	–41.58	–0.05	–0.02
Co	0.025	14991.7	0.2951	0.36	**0.32**	–40.83	–0.10	**–0.14**
Fe	0.06	1207.6	0.3084	1.05	**0.94**	–40.12	–0.12	**–0.23**
Mn	0.11	1007.4	0.3262	2.50	**2.26**	–38.73	–0.06	**–0.30**
Ca	0.28	1090.4	0.3437	5.91	**5.35**	–35.95	0.57	**0.01**
Sr	0.46	959.1	0.3721	9.57	**8.74**	–33.42	1.70	**0.87**
Ba	0.63	905.7	0.3976	13.53	**12.47**	–30.67	2.91	**1.85**
Trivalent impurities								
Sc	0.025	1299.4	0.3312	–19.82	**–20.74**	–144.5	2.65	**1.73**
Cr	–0.105	1255.2	0.349	–15.43	**–16.67**	–136.8	3.21	**1.97**
Nd	0.263	1379.9	0.3601	–10.97	**–12.50**	–129.2	3.88	**2.35**
Yb	0.148	1309.6	0.3462	–15.57	**–16.80**	–136.8	3.04	**1.82**
Gd	0.218	1336.8	0.3551	–12.82	**–14.24**	–132.2	3.50	**2.08**
Eu	0.227	1358	0.3556	–12.45	**–13.89**	–131.6	3.57	**2.13**
Ti	–0.05	1715.7	0.3069	–22.88	**–23.60**	–150.4	2.54	**1.82**
Y	0.18	1345.1	0.3491	–14.38	**–15.69**	–134.7	3.22	**1.92**
Pu	0.28	1376.2	0.3593	–11.23	**–12.75**	–129.6	3.82	**2.30**
Tetravalent impurities								
Ce	0.52	1986.8	0.3511	30.90		–104.3	6.46	
Ge	0.13	1035.5	0.3464	9.19		–119.1	–0.44	
Ti	0.16	754.2	0.3879	17.26		–112.5	1.01	
V	0.2	706.882	0.3865	13.88		–114.6	–0.26	
Th	0.6	2201.1	0.357	35.55		–100.4	7.23	
U	0.55	2246.8	0.3554	35.42		–100.6	7.31	
Zr	0.33	1608.1	0.3509	25.55		–108.3	5.10	
Hf	0.32	1454.6	0.35	22.33		–109.4	3.01	

Note: The ionic radii of Ce^{4+}, V^{4+}, Th^{4+}, and U^{4+} were obtained by extrapolating r as a function of the coordination number.

impurities than is the M2 site, except for the large-sized ion Rb^+. In the case of divalent nickel, cobalt, and iron, the difference in solution energy between the octahedral sites is not very large. The solution energy of Ni is lower in the M1 site, and those of Co and Fe are lower in the M2 site. According to the experimental data reported by Rajamani *et al.* [37], these impurities may substitute for Mg on both the M1 and M2 sites but prefer M1, particularly Ni. For the other divalent impurities studied, the solution energy in the M2 site is lower

than that in M1, in accordance with experimental evidence that Ca and Mn ions substitute for Mg primarily on the M2 site [37, 38].

According to our calculations, trivalent impurities must preferentially occupy the M2 site. This conclusion agrees with the EPR data reported by Gaite [39], which indicate that Gd^{3+} occupies the M2 site in forsterite. At the same time, there is ample EPR evidence that Cr^{3+} preferentially occupies the M1 site [40–43]. The Cr^{3+} ions in forsterite substitute for Mg on the M1 and M2 sites in the ratio from 3 : 2 [41] to 9 : 2 [40]. Under oxidizing conditions, this ratio is typically even larger.

Thus, the solution energies of impurities calculated under the assumptions indicated above make it possible, in some cases, to predict the distribution of impurities over lattice sites. Such predictions are, however, not always correct because the cation distribution is governed by a rather complex system of factors. Site preference depends not only on the cation size, charge, and electronegativity, the crystal field, and the nature of the lattice site but also on the growth temperature, the cooling rate of the crystal, and oxygen fugacity. To accurately assess site occupancies, one must take into account the effect of lattice sites on the chemical bonding of a given element and the effect of site symmetry on the energy of crystal-field stabilization of transition-metal atoms [11]. These factors are difficult to take into account in computer simulation.

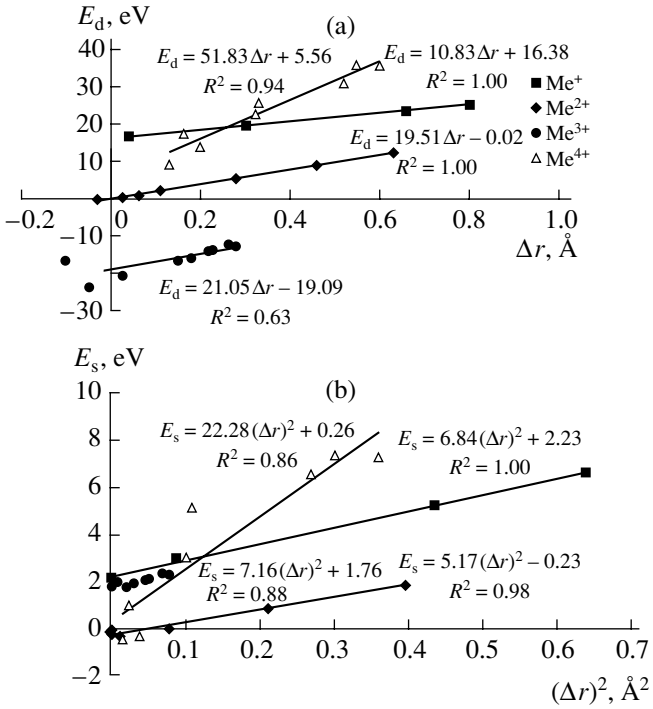

Fig. 5. (a) Energy of impurity defects as a function of Δr; (b) solution energy of impurities in forsterite as a function of $(\Delta r)^2$.

EFFECT OF IMPURITY CATION SIZE AND CHARGE ON THE DEFECT ENERGY AND SOLUTION ENERGY OF IMPURITIES

Figure 5 shows the defect energy and the solution energy of impurities as functions of the difference in ionic radius between the host atoms and the substituent. The ionic radii were taken from [20]. The defect energy and the solution energy of impurities are rated by their minimal values (indicated in bold type in Table 5). The defect energies are best represented by a linear function of Δr, and the solution energies, by a quadratic function.

The best fit equations for the defect energies have the form

$$E_d = 10.83\Delta r + 16.38 \text{ for } Me^+,$$

$$E_d = 19.51\Delta r - 0.02 \text{ for } Me^{2+},$$

$$E_d = 21.05\Delta r - 19.09 \text{ for } Me^{3+},$$

$$E_d = 51.83\Delta r + 5.56 \text{ for } Me^{4+}.$$

In the case of isovalent substitutions ($Me^{\times}_{Mg}$ and $Me^{\times}_{Si}$), the plots of E_d versus Δr pass close to the origin. Thus, replacement of a host ion by an ion of the same charge and close in size has little effect on the total energy of the crystal. In the case of heterovalent substitutions (Me'_{Mg} and $Me^{\cdot}_{Mg}$), the y intercept of the plot of the defect energy versus Δr is about 20 eV in magnitude, which implies that charged impurity defects give rise to significant changes in crystal energy even at small Δr. These changes are comparable to those produced by Mg- and O-related charged native defects in forsterite (Table 5).

The slope of the plot of E_d versus Δr increases in the order $Me^+ < Me^{2+} < Me^{3+} < Me^{4+}$, which indicates that, with increasing impurity cation charge, the defect energy becomes more sensitive to the size mismatch. The plot for monovalent impurities, which typically occupy the M1 site, has the most gradual slope. In the case of divalent and trivalent impurities, which occupy, for the most part, the M2 site, the slope is steeper by about a factor of 2. Finally, the slope for tetravalent impurities is 5 times steeper in comparison with monovalent impurities. These findings may be interpreted as evidence that the tetrahedral site is more rigid than the octahedral sites and that the more heavily distorted octahedral site M2 is more rigid than M1.

Figure 5b shows the solution energy of impurities in forsterite as a function of $(\Delta r)^2$. The best fit equations for these data have the form

$$E_s = 6.84(\Delta r)^2 + 2.23 \text{ for } Me^+,$$

$$E_s = 5.17(\Delta r)^2 - 0.23 \text{ for } Me^{2+},$$

$$E_s = 7.16(\Delta r)^2 + 1.76 \text{ for } Me^{3+},$$

$$E_s = 22.28(\Delta r)^2 + 0.26 \text{ for } Me^{4+}.$$

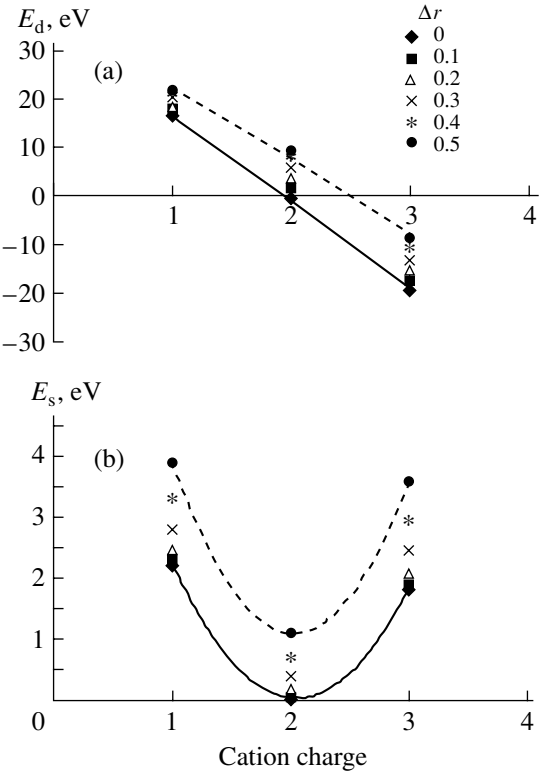

Fig. 6. (a) Defect energy and (b) solution energy of impurities in forsterite as a function of the charge on the impurity cation in the Mg site at different Δr values.

The plots of E_s versus $(\Delta r)^2$ for isovalent substitutions pass close to the origin. For heterovalent substitutions (Me'_{Mg} and $Me^{\cdot}_{Mg}$), the *y* intercept is about 2 eV, which is comparable to the formation energy of charge compensators. As estimated above, the formation energy of Frenkel defects in forsterite is 3.7 eV.

Table 7. Calculated solution energies of trivalent impurities in forsterite in the cases of impurity–vacancy complex formation and compensation doping

Me	E_d, eV	E_s, eV	E_s, eV		
	complexes		Li'_{Mg}	Na'_{Mg}	Al'_{Si}
Sc	–19.70	0.45	0.27	1.07	3.31
Cr	–11.60	0.67	0.51	1.31	3.55
Nd	–3.30	1.03	0.88	1.68	3.92
Yb	–11.90	0.49	0.35	1.15	3.39
Gd	–6.80	0.74	0.61	1.41	3.65
Eu	–6.10	0.80	0.66	1.46	3.70
Ti	–25.50	0.50	0.35	1.15	3.39
Y	–9.70	0.59	0.45	1.25	3.49
Pu	–3.81	0.97	0.83	1.64	3.88

According to Eqs. (6) and (7), compensation of an excess charge on impurity cations requires half as many doubly charged native defects. As shown in an earlier study [44], the *y* intercept of the plot of E_s versus $(\Delta r)^2$ for divalent impurities in alkali halides is 1 eV, which is comparable to the formation energy of the most energetically favorable defects (Schottky defects), which act as charge compensators.

At constant Δr, E_d is a linear function of the cation charge, while E_s varies quadratically (Fig. 6). Increasing Δr increases both E_d and E_s.

Table 7 lists the estimated defect energies and solution energies of trivalent impurities complexed with vacancies. The energy sum in Eq. (12) was replaced by the energy of the defect complex. As follows from the data in Table 7, this ensures an appreciable energy gain, which implies that native defects must attract impurities. Also given in Table 7 are the solution energies of trivalent impurities in the case of compensation doping [Eqs. (8) and (9)]. The solution energy of Me^{3+} decreases upon the introduction of charge compensators in the order $Al'_{Si} > Na'_{Mg} > Li'_{Mg}$. The last two dopants ensure more favorable dissolution conditions compared to compensating vacancies. The most energetically favorable process is the dissolution of trivalent impurities with compensation doping by Li ions, which reduce the solution energy of chromium in forsterite to 1.5 eV. The concurrent formation of $(Me_{Mg}\ Li_{Mg})^{\times}$ defect complexes may ensure a further energy gain on the order of several tenths of an electronvolt.

THERMODYNAMIC ANALYSIS OF IMPURITY PARTITION COEFFICIENTS

A comparison of the $\ln K$ versus $(\Delta r)^2$ and E_s versus $(\Delta r)^2$ data in Figs. 2 and 5b indicates that *K* decreases with increasing E_s, as would be expected. Heterovalent impurities have low *K* and high E_s even at small Δr. The plot of $\ln K$ versus $(\Delta r)^2$ passes rather far from the origin, which may be interpreted in terms of the energy needed for the formation of a charge compensator. Earlier experimental work [45] has shown that concurrent dissolution of chromium and lithium increases the forsterite–melt partition coefficient of Cr by a factor of 1.5 and that of Li by a factor of 2, which correlates with the predicted reduction in the solution energy by 1.5 eV for chromium and by 1.7 eV for lithium. These results provide additional evidence that the partition coefficient is strongly correlated with the solution energy of impurities.

The best fit equations for the $\ln K$ versus E_s data (Fig. 7) have the form

$$-kT\ln K = 0.63E_s + 0.33 \text{ for } Me^{2+},$$

$$-kT\ln K = 1.37E_s - 2.27 \text{ for } Me^{3+},$$

$$-kT\ln K = 0.14E_s + 0.50 \text{ for } Me^{4+}.$$

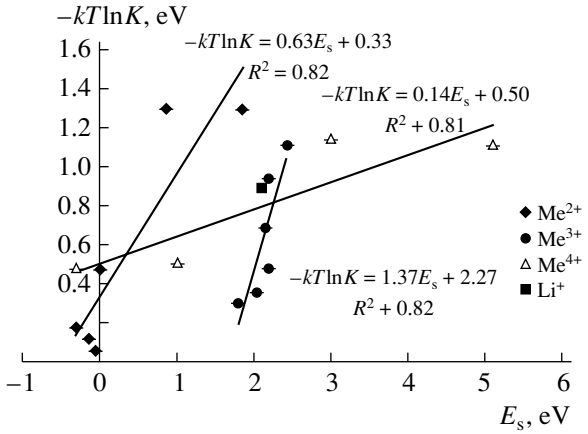

Fig. 7. Correlation between the forsterite–melt partition coefficients of impurities in different valence states and the solution energy of the impurities in forsterite crystals.

The slope of the lines increases in the order $Me^{4+} < Me^{2+} < Me^{3+}$. The *y* intercept is no greater than 0.5 eV for isovalent substitutions and is much larger in magnitude (–2.3 eV) for trivalent impurities. It is reasonable to assume that the calculated static solution energy of impurities is close to their solution enthalpies in dilute solutions at the crystallization temperature [3]. The *y* intercept then represents the entropy contribution to the free energy of solution of the impurity. In the case of heterovalent substitutions, the entropy contribution is substantially larger in comparison with isovalent substitutions, which seems to be associated with the formation of extra defects maintaining electroneutrality.

CONCLUSIONS

The forsterite–melt partition coefficients were determined experimentally and systematized for a large number of mono-, di-, tri-, and tetravalent impurities.

The formation of native defects and dissolution of impurities in forsterite were studied using computer simulation.

The partition coefficient and solution energy of impurities in forsterite were shown to correlate with the difference in ionic radius between the host and substituent atoms. In addition, a strong correlation between *K* and E_s was found.

The partition coefficients of impurities depend primarily on their solution energy, which, in turn, is a function of the differences in ionic radius and valence between the host and impurity atoms. This determines the general trends in the dependences of the principal characteristics of impurities (partition coefficient, solution energy, charge-compensation behavior) on the fundamental crystal-chemical parameters of the host and guest cations.

ACKNOWLEDGMENTS

We are grateful to A.V. Gutina and A.V. Gaister for their assistance with this study.

This work was supported by the Russian Foundation for Basic Research, project nos. 02-02-16360, 02-05-64845, NSh-1955.2003.5, and NSh-493.2003.2.

REFERENCES

1. Nisel'son, L.A. and Yaroshevskii, A.G., *Mezhfazovye koeffitsienty raspredeleniya. Ravnovesiya kristall–zhidkost' i zhidkost'–par* (Partition Coefficients for Solid–Liquid and Liquid–Vapor Equilibria), Moscow: Nauka, 1992.
2. Urusov, V.S., Tauson, V.L., and Akimov, V.V., *Geokhimiya tverdogo tela* (Geochemistry of Solids), Moscow: GEOS, 1997.
3. Allan, N.L., Blundy, J.D., Purton, J.A., *et al.*, Trace Element Incorporation in Minerals and Melts, *EMU Notes Mineral.*, 2001, vol. 3, pp. 251–302.
4. Purton, J.A., Blundy, J.D., and Allan, N.L., Computer Simulation of High-Temperature Forsterite–Melt Partitioning, *Am. Mineral.*, 2000, vol. 85, pp. 1087–1091.
5. *Kristallizatsiya iz rasplavov: Spravochnik* (Crystal Growth from the Melt: A Handbook), Bartel, I., *et al.*, Eds., Moscow: Metallurgiya, 1987.
6. Onuma, N., Higuchi, H., Wakita, H., and Nagasawa, H., Trace Element Partition between Two Pyroxenes and the Host Lava, *Earth Planet. Sci. Lett.*, 1968, vol. 5, pp. 47–51.
7. Jensen, B.B., Patterns of Trace Element Partitioning, *Geochim. Cosmochim. Acta*, 1973, vol. 37, pp. 2227–2242.
8. Philpotts, J.A., The Law of Constant Rejection, *Geochim. Cosmochim. Acta*, 1978, vol. 42, pp. 909–920.
9. Beattie, P., Systematics and Energetics of Trace-Element Partitioning between Olivine and Silicate Melts: Implications for the Nature of Mineral/Melt Partitioning, *Chem. Geol.*, 1994, vol. 117, pp. 57–71.
10. Dudnikova, V.B., Zharikov, E.V., Urusov, V.S., *et al.*, Effects of the Ionic Radius and Charge State of Impurities on Their Forsterite–Melt Partition Coefficient, *Mater. Elektron. Tekh.*, 2000, no. 2, pp. 11–14.
11. Urusov, V.S., *Teoriya izomorfnoii smesimosti* (Theory of Isomorphous Miscibility), Moscow: Nauka, 1977.
12. Blundy, J.D. and Wood, B.J., Prediction of Crystal–Melt Partition Coefficients from Elastic Moduli, *Nature* (London), 1994, vol. 372, pp. 452–454.
13. Wood, B.J. and Blundy, J.D., A Predictive Model for Rare Earth Element Partitioning between Clinopyroxene and Anhydrous Silicate Melt, *Contrib. Mineral. Petrol.*, 1997, vol. 129, pp. 166–181.
14. Blundy, J.D., Robinson, J.A.C., and Wood, B.J., Heavy REE Are Compatible in Clinopyroxene on the Spinel Iherzolite Solidus, *Earth Planet. Sci. Lett.*, 1998, vol. 160, pp. 493–504.
15. Blundy, J.D. and Dalton, J.A., An Experimental Comparison of Clinopyroxene–Melt Partitioning in Silicate and Carbonate Systems and Implications for Mantle Metasomatism, *Contrib. Mineral. Petrol.*, 2000, vol. 139, pp. 356–371.

16. Brenan, J.M., Shaw, H.F., Ryerson, F.J., and Phinney, D.L., Experimental Determination of Trace Element Partitioning between Pargasitic Amphibole and Synthetic Hydrous Melt, *Earth Planet. Sci. Lett.*, 1995, vol. 135, pp. 1–12.

17. La Tourette, T., Hervig, R.L., and Holloway, J.R., Trace Element Partitioning between Amphibole, Phlogopite, and Basanite Melt, *Earth Planet. Sci. Lett.*, 1995, vol. 135, pp. 13–30.

18. Möller, P., The Dependence of Partition Coefficients on Differences of Ionic Volumes in Crystal–Melt Systems, *Contrib. Mineral. Petrol.*, 1988, vol. 99, pp. 62–69.

19. Dudnikova, V.B., Urusov, V.S., Bykov, A.B., and Kolesov, G.M., Forsterite–Melt Partitioning of Trivalent Trace Elements, *Geokhimiya*, 1992, no. 3, pp. 444–447.

20. Shannon, R.D., Revised Effective Ionic Radii and Systematic Studies of Interatomic Distances in Halides and Chalcogenides, *Acta Crystallogr., Sect. A: Cryst. Phys., Diffr., Theor. Gen. Crystallogr.*, 1976, vol. 32, no. 5, pp. 751–767.

21. Dudnikova, V.B., Zharikov, E.V., Eremin, N.N., *et al.*, Forsterite–Melt Partitioning of Vanadium and the Structural and Valence States of Vanadium, *Geokhimiya,* 2001, no. 7, pp. 734–743.

22. Dudnikova, V.B., Gaister, A.V., Zharikov, E.V., *et al.*, Forsterite–Melt Partitioning of Cr at Different Redox Conditions and Cr Concentrations in the Melt, *Geokhimiya*, 2005, no. 5.

23. Shenjun, L., Lin, L., Zulun, W., *et al.*, Growth and Characteristics of Mg_2SiO_4:Ti Crystal, *J. Cryst. Growth,* 1994, vol. 139, pp. 327–331.

24. Kobayashi, T. and Takei, H., Distribution of Some Trivalent Ions between Melt and Single Crystals Mg_2SiO_4 Grown by Czochralski Method, *Earth Planet. Sci. Lett.*, 1977, vol. 36, pp. 231–236.

25. Wood, B.J. and Blundy, J.D., The Effect of Cation Charge on Crystal–Melt Partitioning of Trace Element, *Earth Planet. Sci. Lett.*, 2001, vol. 188, pp. 59–71.

26. Birle, I.D., Gibbs, G.V., Moore, P.B., and Smith, J.V., Crystal Structure of Natural Olivines, *Am. Mineral.,* 1968, vol. 53, pp. 807–825.

27. Gale, J.D., GULP: A Computer Program for the Symmetry Adopted Simulation of Solids, *J. Chem. Soc., Faraday Trans.*, 1997, vol. 93, pp. 629–637.

28. Freeman, C.M. and Catlow, C.R.A., A Computer Modeling Study of Defect and Dopant States in SnO_2, *J. Solid State Chem.*, 1990, vol. 85, pp. 65–75.

29. Lewis, G.V. and Catlow, C.R.A., Potential Models for Ionic Oxides, *J. Phys. C: Solid State Phys.*, 1985, vol. 18, pp. 1149–1161.

30. Sanders, M.J., Leslie, M.J., and Catlow, C.R.A., Interatomic Potentials for SiO_2, *J. Chem., Soc. Chem. Commun.*, 1984, vol. 18, pp. 1271–1273.

31. Hazen, R.M., Effects of Temperature and Pressure on the Crystal Structure of Forsterite, *Am. Mineral.*, 1976, vol. 61, pp. 1280–1293.

32. Smyth, D.M. and Stocker, R.L., Point Defects and Non-Stoichiometry in Forsterite, *Phys. Earth Planet. Inter.*, 1975, vol. 10, pp. 183–192.

33. Andersson, K., Borchart, G., Scherrer, S., and Weber, S., Self Diffusion in Mg_2SiO_4 (Forsterite) at High Temperature: A Model Case Study for SIMS Analyses on Ceramic Surfaces, *Fresenius' J. Anal. Chem.*, 1989, vol. 333, pp. 383–385.

34. Jaoul, O., Bertran-Alvarez, Y., Liebermann, R.C., and Price, G.D., Fe–Mg Interdiffusion in Olivine up to 9 GPa at T = 600–900°C; Experimental Data and Comparison with Defect Calculations, *Phys. Earth Planet. Inter.,* 1995, vol. 89, pp. 199–218.

35. Purton, J.A., Allan, N.L., Blundy, J.D., and Wasserman, E.A., Isovalent Trace Element Partitioning between Minerals and Melts: A Computer Simulation Study, *Geochim. Cosmochim. Acta*, 1996, vol. 60, pp. 4977–4987.

36. Purton, J.A., Allan, N.L., and Blundy, J.D., Calculation Solution Energies of Heterovalent Cations in Forsterite and Diopside: Implication for Trace Element Partitioning, *Geochim. Cosmochim. Acta*, 1997, vol. 61, pp. 3927–3936.

37. Rajamani, V., Brown, G.E., and Prewitt, C.T., Cation Ordering in Ni–Mg Olivine, *Am. Mineral.*, 1975, vol. 60, pp. 292–299.

38. McCormick, T.C., Smyth, J.R., and Lofgren, G.E., Site Occupancies of Minor Elements in Synthetic Olivines as Determined by Channeling-Enhanced X-ray Emission, *Phys. Chem. Miner.*, 1987, vol. 14, pp. 368–372.

39. Gaite, J.M., Pseudo-Symmetries of Crystallographic Coordination Polyhedra. Application to Forsterite and Comparison with Some EPR Results, *Phys. Chem. Miner.*, 1980, vol. 6, pp. 9–17.

40. Mass, J.L., Burlitch, J.M., Markgraf, S.A., *et al.*, Oxygen Activity Dependence of Chromium(IV) Population in Chromium-Doped Forsterite Crystals Grown by Floating Zone Technique, *J. Cryst. Growth*, 1996, vol. 165, pp. 250–257.

41. Rager, H., Electron Spin Resonance of Trivalent Chromium in Forsterite, Mg_2SiO_4, *Phys. Chem. Miner.*, 1977, vol. 1, pp. 371–378.

42. Rager, H., Electron–Nuclear Hyperfine Interaction of $^{53}Cr^{3+}$ in Mg_2SiO_4 (Forsterite), *Z. Naturforsch., A*, 1980, vol. 3, pp. 1296–1303.

43. Budil, D.E., Park, D.G., Freed, J.H., *et al.*, 9.6 GHz and 34 GHz Electron Paramagnetic Resonance Studies of Chromium-Doped Forsterite, *J. Chem. Phys.*, 1994, vol. 101, pp. 3538–3548.

44. Urusov, V.S. and Dudnikova, V.B., Energetics of Heterovalent Microisomorphism with Vacancy Formation in Ionic Crystals, *Geokhimiya*, 1987, no. 9, pp. 1219–1230.

45. Dudnikova, V.B., Gaister, A.V., Zharikov, E.V., *et al.*, Effect of Compensation Doping on Chromium Solubility in Forsterite, *Neorg. Mater.*, 2003, vol. 39, no. 8, pp. 985–990 [*Inorg. Mater.* (Engl. Transl.), vol. 39, no. 8, pp. 845–850].